Characterization and analysis of the mode I interlaminar fatigue behaviour of thermoplastic composites considering R-curve effects

Leciñana, I.; Renart, J.; Turon, A.; Zurbitu, J.; Tijs, B. H.A.H.

DOI
10.1016/j.engfracmech.2023.109273

Publication date
2023

Document Version
Final published version

Published in
Engineering Fracture Mechanics

Engineering Fracture Mechanics 286 (2023) 109273

Contents lists available at ScienceDirect

Engineering Fracture Mechanics

journal homepage: www.elsevier.com/locate/engfracmech

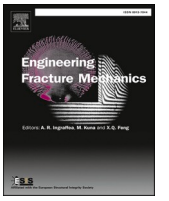

Characterization and analysis of the mode I interlaminar fatigue behaviour of thermoplastic composites considering $\mathscr{R}$-curve effects

I. Leciñana [a,b], J. Renart [b,*], A. Turon [b], J. Zurbitu [a], B.H.A.H. Tijs [c,d,*]

[a] IKERLAN Technology Research Centre, Basque Research and Technology Alliance (BRTA), Gipuzkoa, Spain
[b] AMADE, Polytechnic School, University of Girona, Girona, Spain
[c] Fokker/GKN Aerospace, Papendrecht, The Netherlands
[d] Faculty of Aerospace Engineering, Delft University of Technology, Delft, The Netherlands

ARTICLE INFO

Keywords:
Fatigue characterization
Fibre bridging
Resistance curve
Fatigue cohesive zone model

ABSTRACT

Through the application of innovative production processes, thermoplastic composites might help the aviation industry become more sustainable. However, there is currently not much experimental understanding on the fatigue behaviour, and validated analysis methodologies on thermoplastic composites are rather limited. In this work, the fatigue onset and propagation interlaminar properties of AS4D/PEKK-FC thermoplastic composite were characterized under mode I loading. Testing costs were reduced by using a multi-fatigue testing rig that allows loading 6 specimens at the same time. The offset in the fatigue crack growth rate curves tested at different severities was explained by the fatigue $\mathscr{R}$-curve effects. The offset was modelled by means of superposed fatigue cohesive laws. Different approaches on how to consider fatigue damage were compared with experimental data, giving an insight on how fatigue damage evolves, and developing a novel modelling strategy based on a robust method for fatigue model parameter identification for fatigue delamination when several failure mechanisms interact.

1. Introduction

Thermoplastic composites may enable a more sustainable aviation industry using new manufacturing techniques. New generation of thermoplastic resins, such as the Poly (Ether-Ketone-Ketone) (PEKK) have an increased crystallization rate and lower the melting temperature compared to other high performance thermoplastics, benefiting cost-efficient and high-volume manufacturing. In addition, thermoplastic polymers have better damage tolerance to impacts and better environmental and solvent resistance than thermosets [1], because of their improved fracture toughness and more ductile behaviour.

One of the key points in the analysis of structures for the transportation sector is to have reliable data under service conditions. In composite structures, having information about the interlaminar properties under cyclic loading is crucial for an accurate estimation of the service life of the component. However, the amount of work done in fatigue with thermoplastic composites is rather limited and mainly concern the PEEK in mode I [2–6]. There is no available data for AS4D/PEKK-FC under fatigue. The only available data is the work from Tijs et al. [7] focused on the analysis of PEKK-FC [8] under static loading. The results of Tijs et al. work [7] shows that the

* Corresponding authors.
E-mail addresses: jordi.renart@udg.edu (J. Renart), bas.tijs@fokker.com (B.H.A.H. Tijs).

https://doi.org/10.1016/j.engfracmech.2023.109273
Received 31 January 2023; Received in revised form 3 April 2023; Accepted 14 April 2023
Available online 17 April 2023

material exhibits a significant amount of fibre bridging during the fracture process and a strategy based on a multilinear cohesive law was proposed to simulate the static fracture. However, it is observed that in fatigue, the fibre-bridging has a strong influence on the crack growth rate curves [6,9–13] and there is limited work in the literature to simulate this influence.

To reduce costs during the certification processes, it is of great interest to substitute some of the upper part of the testing pyramid by analysis methods and simulation strategies such as virtual testing [14]. For that propose, predictive tools must be capable of accurately modelling the failure mechanisms.

Carreras *et al.* presented a global fatigue cohesive zone model (FCZM) base on Pariś law equations that proved to yield consistent predictions for a 3D thermoset structure [15]. The model is based on the concepts of crack growth driving direction and evaluation of mode-decomposed energy release rate [16,17]. A sensitivity analysis made in [18] concluded that this model is insensitive to the static cohesive law and only dependent on the fatigue crack growth equation with which is fed. This implies that a) fatigue onset response is not correlated with experimental data and b) if the fatigue crack growth behaviour of the material is influenced by its resistance curve ($\mathscr{R}$-curve), as it is the case in AS4D/PEKK-FC material [7], specific experimental data regarding the crack growth law in non-fully developed regimes should be provided.

Alternatively, Dávila *et al.* developed a local CZM inspired on S-N curves [19,20] that links the damage rate dD/dN to the static cohesive law. Additionally, a robust fatigue parameter determination method was developed in [21], that allows determining the model fatigue inputs from fatigue onset and propagation characterization data. The predictive capabilities of the model in conjunction with the parameter determination method was validated in a 3D thermoset benchmark test, showing potential to intrinsically account for effects that modify crack propagation curves such as adherent thickness or $\mathscr{R}$-curve effects.

In this work, the fatigue onset and propagation behaviour of a AS4D/PEKK-FC thermoplastic composite under mode I loading is characterized, including fatigue $\mathscr{R}$-curve effects. The influence of the $\mathscr{R}$-curve under fatigue loading is evaluated by means of a fatigue cohesive zone model [20], focusing on how the combination of different failure mechanisms such as fracture, plasticity, and/or fibre bridging have an impact in the fatigue $\mathscr{R}$-curve effects. As a result, a modelling strategy that considers $\mathscr{R}$-curve effects in both static and fatigue response is proposed extending the multilinear cohesive law presented by Tijs et al. [7].

2. Experimental methodology

2.1. Material properties

The material used in this work is the Solvay (formerly Cytec) APC (PEKK-FC) thermoplastic polymer prepreg which consists of a fast-crystallizing thermoplastic matrix of poly ether-ketone-ketone commonly referred to as PEKK-FC, reinforced with a continuous unidirectional AS4D fibre with a nominal ply thickness of 0.138 mm. In Table 1 the elastic and interlaminar properties used in the data reduction are summarized, for more information, the reader may refer to [7].

2.2. Specimen design

An AS4D/PEKK-FC laminate that consists of 30 unidirectional plies was manufactured through autoclave consolidation and specimens for mode I fatigue tests were machined. The specimens were designed to be 25 mm wide and 225 mm long. Due to the high melting temperature of thermoplastic composites, a 12.5mu thick UPILEX foil (60 mm long) was used as insert to start the crack.

2.3. Fatigue tests

A fatigue testing campaign was performed to obtain onset and crack growth rate curves in mode I at AMADE testing facilities of the University of Girona (UdG). The tests were run under displacement control at a displacement ratio of $R_d = \delta_{min}/\delta_{max} = 0.1$ and test frequency of 5 Hz. The run-out was set to $2{\cdot}10^6$ cycles. The tests were performed in laboratory conditions at 23 ± 2 °C and at a RH of 50 ± 5 %.

To reduce the testing times, the fatigue tests were carried out in a multi-fatigue test device capable of testing 6 specimens in parallel at the same time [22] as shown in Fig. 1. The same displacement was applied to all the specimens, but the load was measured individually by 2 kN load cells.

During the test, the load and displacement of each specimen were recorded at a frequency of 100 Hz with an external system from HBM (model Quantum MX1615), having 20 points per cycle. For each cycle, the dynamic compliance (C) was computed from the linear regression between the load and displacement data points of each cycle. The crack length (a) at each cycle was estimated by

Table 1
AS4D/PEKK-FC thermoplastic composite elastic and static interlaminar properties at room temperature [7].

Property	Description	Value	Unit
E_{1t}	Young's modulus, fibre tensile direction	138,300	MPa
E_{2t}	Young's modulus, matrix tensile direction	10,400	MPa
$G_{12} = G_{13}$	Shear modulus	5190	MPa
$\mathscr{G}_{Ic,i}$	Mode I interlaminar fracture toughness, initiation	0.7	kJ/m^2
$\mathscr{G}_{Ic,p}$	Mode I interlaminar fracture toughness, propagation	1.12	kJ/m^2

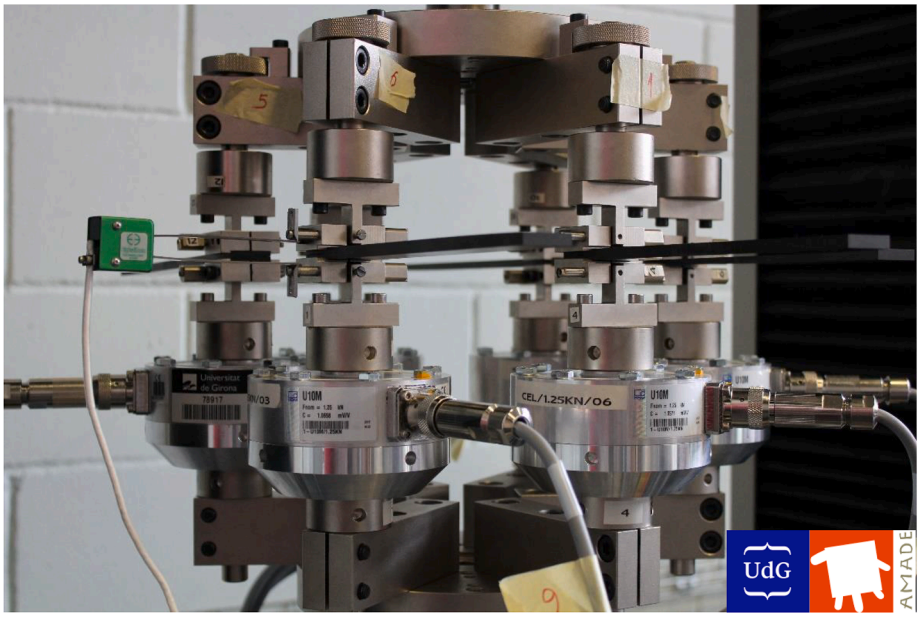

Fig. 1. Multi-fatigue test device capable of testing 6 DCB specimens in parallel [22].

relating C to a from a series of compliance calibration tests [22]. The compliance calibration tests consist of loading and unloading the specimens at different crack lengths before the cyclic tests. An scheme of the procedure is shown in Fig. 2, where the same specimen is loaded until P_{max} at the following crack lengths: a_p (Fig. 2, (1)), a_p – 4 mm, a_p – 8 mm, a_p – 12 mm, and a_p – 16 mm (Fig. 2, (2)). To facilitate the attachment and detachment of the loading blocks to the specimen, mechanical side clamped blocks were used [22,23].

The crack length was estimated through specimen compliance:

$$C^{1/3} = m(a + \Delta) \tag{1}$$

where Δ is the crack length correction [1], and m the slope of the curve.

The specimens were tested at the same displacement ratio (R_d) but at different levels of the maximum initial energy release rate ($\mathcal{G}_{Imax0}$) by changing the initial crack length of each specimen (a_0):

$$a_0 = \left(\frac{3\delta_{max}^2}{2Bm^3\,\mathcal{G}_{Imax0}}\right)^{1/4} - \Delta \tag{2}$$

where, δ_{max} is the maximum displacement applied and B the specimen width. The energy release rate was computed at each cycle by the Corrected Beam Theory data reduction method:

$$\mathcal{G}_I = \frac{3P\delta}{2B(a+\Delta)} \tag{3}$$

where the $\mathcal{G}_{Imax}$ and $\mathcal{G}_{Imin}$ were obtained from $\delta = \delta_{max}$ and $P = P_{max}$, and $\delta = \delta_{min}$ and $P = P_{min}$, respectively.

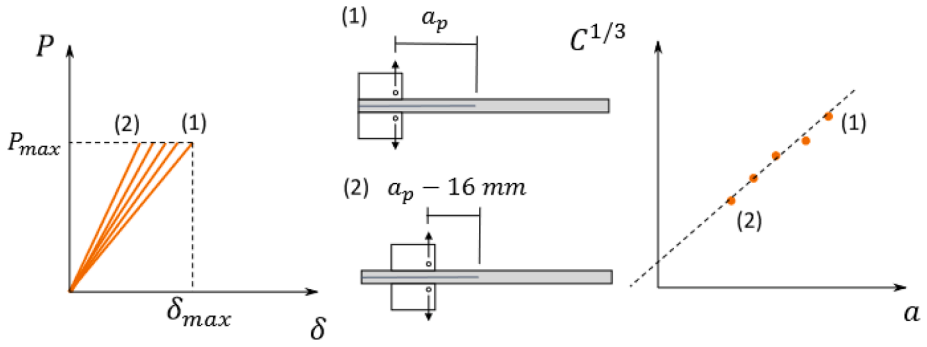

Fig. 2. Dynamic compliance calibration test procedure.

For more details about the test rig and data reduction procedure, the reader may refer to [22].

3. Numerical methodology

This section describes the numerical strategy to account for fatigue $\mathscr{R}$-curve effects. First, an approach to capture fatigue $\mathscr{R}$-curve effect is proposed, in which experimental fatigue onset and propagation data is synthesized into four experimental constants for each test. The static fracture is modelled by superposing multiple cohesive laws that capture the static $\mathscr{R}$-curve effect [7]. Then, several strategies to accumulate fatigue damage are discussed considering the physical representation of each of the superposed cohesive law. The fatigue parameters for each damage accumulation strategy were set to accurately capture the four experimental fatigue constants taking a single experiment as reference. Finally, a modelling strategy that considers static and fatigue $\mathscr{R}$-curve effects is proposed after evaluating the fatigue damage accumulation strategies based on the global modelling accuracy of all the fatigue tests.

3.1. Fatigue cohesive zone model formulation

The CF20 FCZM [20] is built in a static CZM formulated by Turon *et al.* [24] that can accurately predict delamination onset and growth under variable mixed-mode loading conditions. The model consists of a bilinear traction-separation softening law that relates the mode equivalent traction (τ) to the mixed-mode equivalent displacement jump λ as a function of a damage variable d (Fig. 3a). Damage initiation is related to the interfacial strength of the material τ_0 by a penalty stiffness K, which value gets decreased as the damage variable evolves:

$$\tau = (1-d)K\lambda \tag{4}$$

The dissipated energy per surface area during the damage process is bounded by the fracture toughness of the material, G_C, which is equal to the area under the traction-separation law. The energetic damage variable D quantifies the ratio between the energy dissipated per surface area and the fracture toughness $\mathscr{G}_C$. It is related to the stiffness damage variable d by:

$$d = \frac{D\lambda_C}{D\lambda_C + (1-D)\lambda_0} \tag{5}$$

The parameters that define the mixed-mode cohesive law are calculated locally as a function of the Benzeggagh and Kenane interpolation criteria [25], pure-mode properties, and the local mixed mode ratio B. Thermodynamical consistency is ensured thanks to the mode-dependent penalty stiffness definition developed in [24].

To account for fatigue damage, the S-N curve based fatigue CZM presented by Davila *et al.* [20] is implemented in the static CZM. This way the static cohesive law becomes the envelope of fatigue damage: Even if the displacement jump of a material point is lower than the static onset value, damage is accumulated because of fatigue loading (Fig. 3b from point A to F). When reaching point F, the material point will catastrophically fail because of load-carrying inability. Both fatigue onset and propagation can be modelled using pointwise information (at integration point level). The fatigue input parameters of the model are the relative endurance limit of the material under mode I fully reversed loading (ε), the brittleness parameter (η) and the nondimensional material dependent coefficient (p). ε influences the slope of both S-N curves and fatigue propagation laws. η accounts for the fatigue resistance rise that some materials exhibit during the low cycle fatigue. p has an impact on the Paris law coefficient C and in the fatigue onset. To account for the stress ratio R and the mode mixity B, the endurance limit (E) is derived as a function of the Goodman relation:

$$E = \frac{2C_L\varepsilon}{C_L\varepsilon + 1 + (C_L\varepsilon - 1)R} \tag{6}$$

where $C_L = 1 - 0.42B$.

The fatigue damage accumulation function is defined by the local displacement jumps, λ, and model fatigue input parameters:

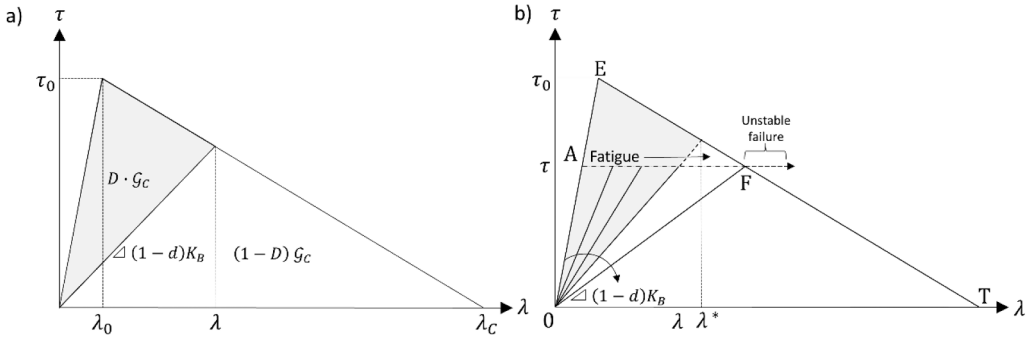

Fig. 3. A) representation of the bilinear cohesive law used in the formulation for a fixed mode ratio[24] b) fatigue damage accumulation under subcritical traction.

$$\frac{dD}{dN} = \frac{1}{\gamma}\frac{(1-D)^{\beta-p}}{E^{\beta}(p+1)}\left(\frac{\lambda}{\lambda^{*}}\right)^{\beta} \tag{7}$$

where D is the energetic damage variable, λ^{*} is the equivalent displacement jump that would onset static tearing, and γ is the number of cycles at which infinite live is considered.

To increase efficiency in fatigue crack growth calculations, load envelope strategy was implemented. The cycle jump per iteration, ΔN, was calculated:

$$\Delta N = \frac{\Delta D_{\max}}{\max\limits_{j\in CZ}\left\{\frac{\partial D_{\text{fat.j.}}}{\partial N}\right\}} \tag{8}$$

where $\Delta D_{\max}$ is the maximum damage increment allowed by the user and $\max\limits_{j\in CZ}\left\{\frac{\partial D_{\text{fat.j.}}}{\partial N}\right\}$ is the highest fatigue damage rate of all the integration points j undergoing damage, i.e., in the cohesive zone (CZ), in the previous iteration. This way it is ensured that no material point exceeds the maximum allowable damage increment per iteration.

More detailed information of the formulation can be found in references [19,20]. The static and fatigue constitutive models were implemented in a user defined material subroutine for ABAQUS STANDARD (UMAT).

3.2. Characterization of the fatigue response

Experimental data of both fatigue onset and propagation was reduced with the characterization of four fatigue constants:

On the one hand, the load-displacement data until fatigue onset was fitted to a power law equation to represent fatigue onset information:

$$\frac{\delta}{F} = O_A (N_{0.05})^{O_B} \tag{9}$$

where δ and F are the displacement and the reaction force at the loading point of the specimen, O_A and O_B are the fitting parameters, and $N_{0.05}$ is the number of cycles that ranges from 1 until fatigue onset. 5% of compliance increase is taken here because, from the authors experience, it typically ensures full development of the process zone. Especially for relatively ductile polymers and in interfaces with non-neglectable fibre bridging, it is of great importance to capture the damage development before the onset of a crack. Each data point of the loading displacement curve represents the maximum traction point of each fatigue cycle.

On the other hand, the high cycle fatigue response is described by relating the crack growth rate da/dN to the maximum strain energy release rate $\mathscr{G}_{\max}$:

$$\frac{da}{dN} = C\left(\frac{\mathscr{G}_{\max}(1-R)}{\mathscr{G}_{C}}\right)^{m} \tag{10}$$

where m and C are the Paris law constants and R is the displacement ratio imposed during the test ($R = \frac{\delta_{\min}}{\delta_{\max}}$, where $\delta_{\min}$ and $\delta_{\max}$ are de minimum and maximum displacements of the cycle, respectively).

3.3. Fatigue damage accumulation strategy

The resistance curves characterized in [7] proves that AS4D/PEKK-FC material starts developing damage at significantly lower values than the propagation fracture toughness, $\mathscr{G}_{Ic,p}$. Therefore, even if a structure is subjected to subcritical fatigue loading, a material region may be statically damaged before the fatigue damage evolves. Consequently, if non-pre-cracked characterization specimens are subjected to different subcritical fatigue severities, different crack growth laws will be obtained due to the different damage fields within the cohesive zone and the subsequent non-self-similar fatigue damage propagation. This is an example of how $\mathscr{R}$-curve effects may have an impact in the fatigue damage onset and propagation behaviour.

To evaluate the capability of the CF20 FCZM [20] to consider the $\mathscr{R}$-curve effects in the fatigue response, mode I fatigue tests of specimens starting from insert were analysed as a case study. In many applications, a simple bilinear cohesive law can accurately predict crack propagation. However, since various damage mechanism act together in the AS4D/PEKK-FC composite, multiple superposed bilinear cohesive laws (CL) are needed to capture the contribution of the different damage mechanisms. This way, the integral of the cohesive law envelope that results from the addition of the multiple superposed cohesive laws correlates with the $\mathscr{R}$-curve of the material. For the AS4D/PEKK-FC material, the static parameters of each superposed cohesive law were determined in reference [7] (Fig. 4), following the inverse data reduction method based on static load-displacement curves [26,27]. In this study, a total of 5 superposed cohesive laws were used and the static cohesive parameters determined for each cohesive law are defined in Table 2. The shape of the different cohesive laws (CL) and the resulting cohesive law envelope are plotted in Fig. 4. A zoom of CL 4 and 5 was done for a complete overview all the mode I CLs.

The fatigue parameters were determined by correlating the modeĺs fatigue response to a single fatigue severity test under mode I loading by following the methodology proposed in [21]. Different fatigue severities were simulated leaving the fatigue input set unchanged. The fatigue onset and propagation response were correlated against experimental data as validation case study (Table 3).

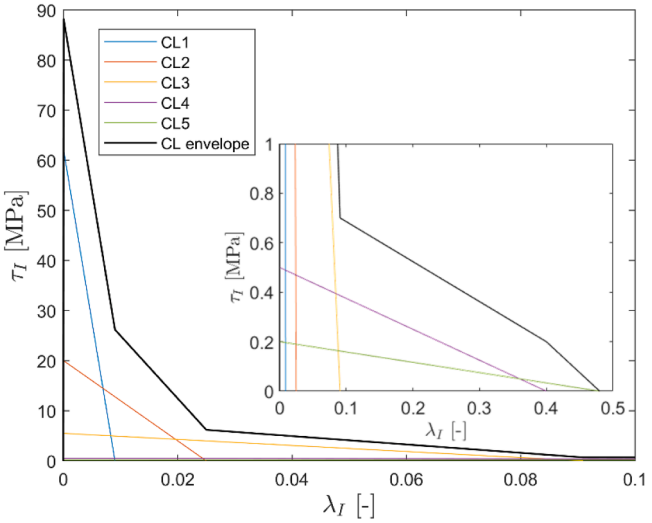

Fig. 4. Multi linear cohesive law resulting from the superposition of the 5 cohesive laws to model $\mathscr{R}$-curve effects such as large-scale fibre bridging.

Table 2
Definition of the superposed static cohesive laws (CL).

	CL1	CL2	CL3	CL4	CL5
τ_{I0}: Mode I static strength [MPa]	62	20	5.5	0.5	0.2
K_I: Mode I penalty stiffness [N/mm^3]	1E6	4.5E5	9.17E4	1.67E4	3.33E3
$\mathscr{G}_{IC}$: Mode I fracture toughness [N/mm]	0.28	0.25	0.25	0.1	0.24

Table 3
Mode I specimens tested and simulated under different severities.

Specimen	Crack-length [mm]	Severity ($\mathscr{G}_{max}/\mathscr{G}_{IC,p}$) [–]	Objective
19–0815	32.05	0.43	Validation
19–0816	33.4	0.38	Validation
19–0817	35.93	0.30	Validation
19–0818	38.05	0.24	Fatigue parameter determination
19–0819	42.97	0.14	Validation

The numerical features and boundary conditions of the models are presented in Table 4.

There are few works in literature that analyse how fatigue damage should be modelled in superposed linear FCZM [28–30]. In all these approaches the same values of the fatigue parameters were used among the different superposed cohesive laws, assuming that all the failure mechanisms that contribute to the $\mathscr{R}$-curve follow the same fatigue accumulation law. However, no physical evidence was followed for this assumption. In fact, Yao et al. stated that there is sufficient evidence that the bridging created in static delamination growth is significantly different from that in fatigue delamination [11]. In this work, different modelling approaches were explored to learn which is the most convenient way to induce fatigue damage in superposed FCL to accurately consider fatigue $\mathscr{R}$-curve effects.

In a first step, the same the fatigue parameters were used in the different superposed cohesive laws (Table 5).

In a second step, fatigue damage was deactivated from the two cohesive laws that represent the toughening effects of low density

Table 4
Numerical features of the numerical models.

Parameter	
l_e: Cohesive element length	0.1 mm
Elements in sub-laminate thickness	8
Element type in beams	CPE4 (Abaqus 6.14–2)
Δd_t: Fatigue damage target per equilibrium iteration	1E-2
Solver	Newton – Raphson NLGEOM static
Cohesive element	COH2D4 + UMAT subroutine
Maximum displacement	2 mm
Minimum displacement	0.2 mm

Table 5
Fatigue law superposition architecture 1 to model the $\mathscr{R}$-curve effects.

Fatigue parameter	FCL1	FCL2	FCL3	FCL4	FCL5
ε	ε	ε	ε	ε	ε
p	p	p	p	p	p
η	η_A	η_A	η_A	η_A	η_A

Table 6
Fatigue law superposition architecture 2 to model the $\mathscr{R}$-curve effects.

Fatigue parameter	FCL1	FCL2	FCL3	FCL4	FCL5
ε	ε	ε	ε	–	–
p	p	p	p	–	–
η	η_A	η_A	η_A	–	–

Table 7
Fatigue law superposition architecture 3 to model the $\mathscr{R}$-curve effects.

Fatigue parameter	FCL1	FCL2	FCL3	FCL4	FCL5
ε	ε	ε	ε	–	–
p	p	p	p	–	–
η	1	η_A	η_B	–	–

long fibre bridging [31] (lower strength values), assuming that under subcritical loadings its fatigue dissipation energy is negligeable (Table 6).

In the last step, the fatigue parameters were allowed to be independent in each superposed cohesive law. It was assumed that the distinct failure mechanisms involved in the $\mathscr{R}$-curve may follow dissimilar fatigue damage development. Allowing different fatigue parameter values in each fatigue cohesive law (FCL), an accurate transition between static and fatigue $\mathscr{R}$-curve effects could be achieved. However, since each FCL is determined by 3 fatigue parameters (ε, η and p), and there are 5 superposed FCL, a total of 15 fatigue parameters must be determined as a function of only 4 experimental fatigue constants (O_A, O_B, m and C). To reduce the number of fatigue parameters, the same value for ε and p parameters were used in all the FCL, assuming that these parameters represent the global effect of several failure mechanisms acting together. To apply different fatigue damage rates, the brittleness parameter (η) was varied among the cohesive laws. In the FCL with higher strength, η was set equal to 1 because it represents the quasi-brittle fracture of the matrix [29,32]. This way, 4 fatigue input parameters must be determined (ε, p, η_A and η_B) as a function of the 4 experimental fatigue constants (O_A, O_B, m and C) (Table 7).

3.4. Determination of the fatigue parameters

Once the problem was defined, the robust fatigue determination method [21] was implemented for each of the proposed cohesive law superposition architectures. The flow chart in Fig. 5 condenses the main features of the methodology.

First the design space is bounded by defining an allowable range for each fatigue input. When defining the range, a compromise between sample size and uncertainty whether the optimal combination is within the limits must be considered (Table 8).

Then, the design space is discretized following a Latin Hypercube Design (LHD) algorithm because of its space-filling and non-collapsing capabilities [33,34]. Having a smoothly sampled design space is crucial to accurately capture the gradients of the non-linear response of the model. The optimal number of design points depends on the non-linearity of the problem. In this case study an initial size of 300 samples was set.

A simulation for each sample point was run with the parametric numerical model, and its fatigue response was reduced to the fatigue onset and propagation constants (O_A, O_B, m and C). A surrogate metamodel was then built for each of the fatigue constants, where the interpolation between the calculated sampled points was established. Gaussian Process based Kriging metamodeling [35] was used for this purpose, being able to estimate the fatigue response of the model for a given set fatigue inputs within the problem boundaries, without the need to compute the numerical solution. The accuracy of the metamodel depends on the sample density and the nonlinearity of the response. Before using the metamodel as a predictive tool for the optimization process, a minimum accuracy was ensured following a *Leave-k-out* verification method.

During the optimization process, a multi-objective genetic algorithm (NSGA-II) [36] was used to find the pareto optimal solution. Finally, the optimum fatigue parameter combination was found within the pareto front after a global error minimization is conducted, selecting the optimal fatigue parameter combination that fits best the experimental fatigue constants:

$$y = \frac{|C_{obj} - C_{predicted}|}{C_{obj}} + 10 \bullet \frac{|m_{obj} - m_{predicted}|}{m_{obj}} + \frac{|O_{Aobj} - O_{Apredicted}|}{O_{Aobj}} + 10 \bullet \frac{|O_{Bobj} - O_{Bpredicted}|}{O_{Aobj}} \tag{11}$$

where *y is* the objective function to minimize, *obj* subindex stands for the experimental fatigue constants and *predicted* subindex refers

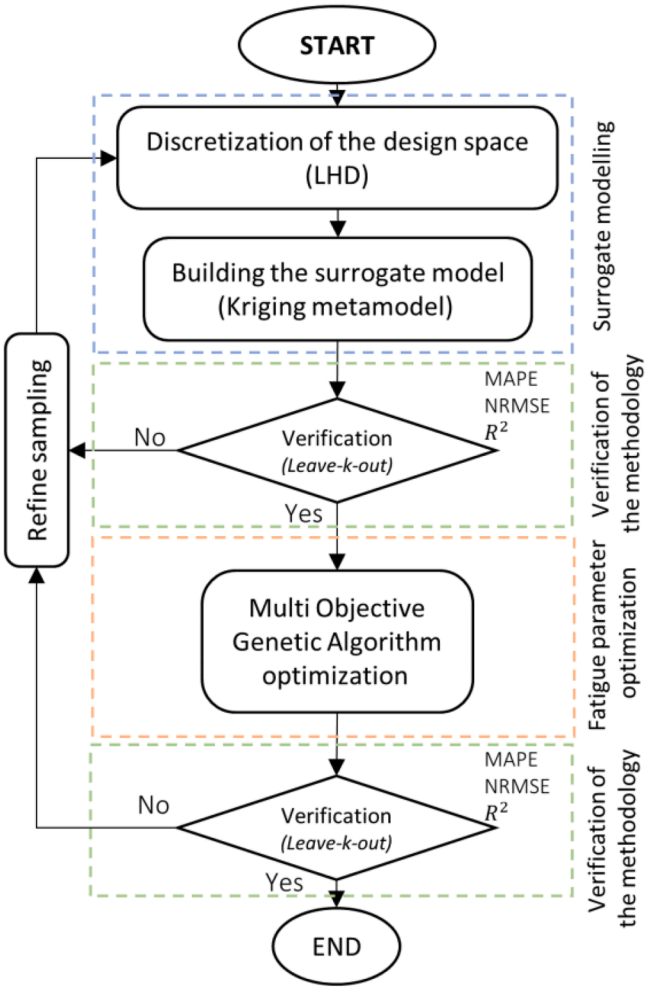

Fig. 5. Flowchart to determine fatigue parameters of the FCZM based on fracture fatigue data [21].

Table 8
Design space bounds for the determination of the fatigue parameters of the FCZM.

Fatigue parameter	Lower bound	Upper bound
ϵ	0.0025	0.25
p	−2.5	2.5
η_A	0.75	0.95
η_B	0.6	0.8

to the predicted values by the metamodel for the input parameter set in each step during the optimization. Since the m and O_B parameters are exponents in eq. (9) and eq. (10), their error was multiplied by a weight of 10 during the global error minimization because its sensitivity in the fatigue response is greater. To see further details of the fatigue parameter method, refer to [21].

4. Experimental characterization

In this section, the characterization of the AS4D/PEKK-FC thermoplastic under fatigue loading is presented. The fatigue onset was evaluated by measuring the number of cycles at which the dynamic compliance of the specimen increased as a function of the maximum strain energy release rate ($\mathcal{G}_{max}$). Three criteria have been taken into account: a 1% and a 5% increase in the compliance, as proposed in the ASTM standard [37], and an intermediate value of a 2% increase [22]. The fatigue propagation was measured by fitting a function of $\mathcal{G}_{max}$ (Eq. (10)) to the crack growth rate.

In Fig. 3 the onset curves of two series of tests with the same type of specimens are plotted: i) tests run directly from the insert; and ii) after a quasi-static pre-crack of 10 mm.

For the same number of cycles, a higher energy release rate is needed to onset the propagation in the tests carried out from the pre-crack (Fig. 6a). The results of the static tests and its micrography, which were reported in [7], shown that this material exhibited plastic deformation and a large amount of fibre bridging. After pre-cracking the specimens, the fibre bridging was fully developed increasing the toughness of the interface, passing from $\mathcal{G}_{Ic,i} = 0.7$ to $\mathcal{G}_{Ic,p} = 1.12$ N/mm. Therefore, if both i) and ii) series of tests are normalized by the propagation fracture toughness ($\mathcal{G}_{Ic,p}$), the tests run from pre-crack shown a better fatigue onset performance. However, if $\mathcal{G}_{\max}$ is rated from the insert tests by $G_{Ic,i}$ and G_{max} from the pre-cracked tests by $G_{Ic,p}$ it is observed that, for this material, all the values fall on the same onset curve (Fig. 6b). Therefore, it can be concluded that the fatigue onset behaviour ($\mathcal{G}_{max}$ *vs* N) can be collapsed in a single curve if experimental data is normalized by the $\mathcal{R}$-curve ($\mathcal{G}_{max}/\mathcal{G}_{IC,\mathcal{R}}$ *vs* N) as a function of the delaminated length, $\mathcal{G}_{IC,\mathcal{R}} = f(a - a_0)$. This is because the fatigue onset is dependent on the failure mechanisms active in a material point. In the tests from insert, the material was undamaged at the beginning of the test, in contrast, failure mechanism such as fibre bridging, and plastic deformation were already developed in the tests from pre-crack.

If the fatigue onset behaviour of the AS4D/PEKK-FC thermoplastic is compared to a high-performance thermoset [22], both fatigue onset performance are similar proportionally to their fracture toughness. Therefore, the fatigue onset performance of the thermoplastic is higher compared to a thermoset since its fracture toughness is higher. Moreover, when additional failure mechanisms are active in the thermoplastic material, its fatigue onset resistance increases.

In Fig. 7., the crack growth rate curves from the specimens tested from the insert and pre-crack are plotted. This does not result in a single curve, but in several parallel curves between tests performed at different severities. This behaviour is typically observed when having fibre bridging in the results [10–13]. For each curve, two phases are clearly identified: a fast crack growth rate region during the first cycles, and a constant crack growth following the Paris-law relationship. These features were both observed in tests run from insert and from pre-crack.

As in the fatigue onset behaviour, tests run from pre-crack experienced a higher fatigue propagation resistance compared to tests run from insert: for the same imposed strain energy release rate, faster crack growth rate was observed in the tests run from insert. An offset in both Paris' law coefficient C and exponent m was observed if applied strain energy release rate $\mathcal{G}_{max}$ is normalized by the

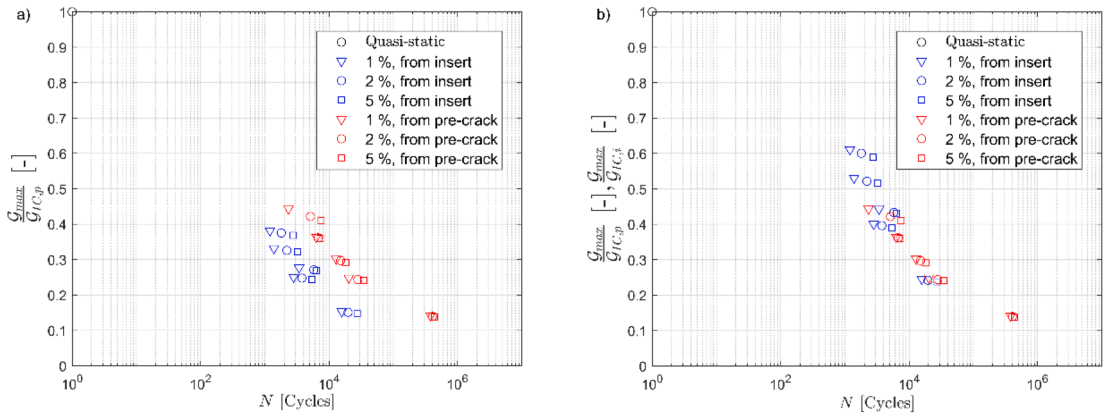

Fig. 6. Fatigue onset tests run from insert and from pre-crack, a) normalized by the propagation toughness and b) normalized by the initiation toughness and propagation toughness respectively.

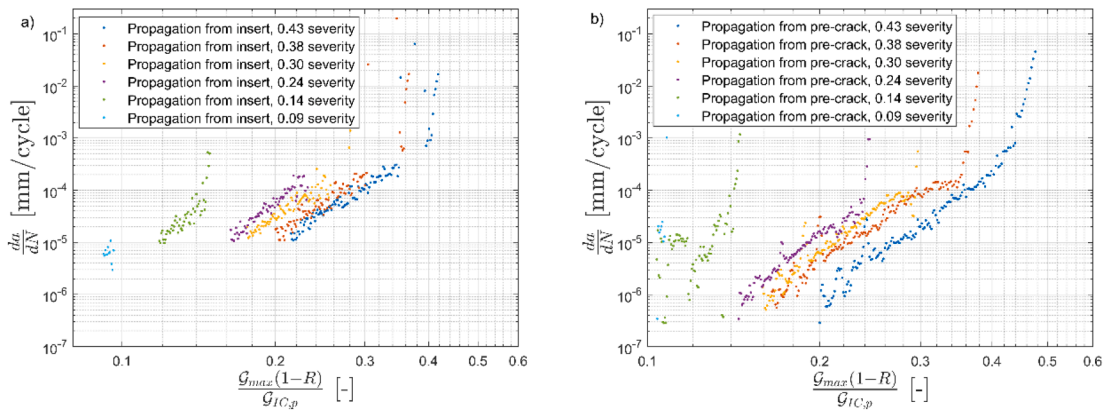

Fig. 7. $\mathcal{R}$-curve effects in fatigue propagation tests run from a) insert and b) from pre-crack, normalized by propagation toughness.

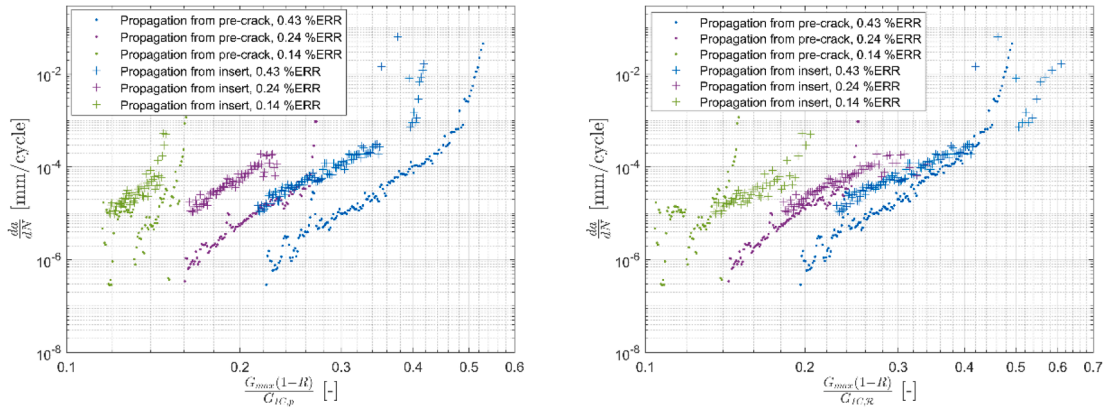

Fig. 8. Comparison of $\mathscr{R}$-curve effects in fatigue propagation tests run from insert and from pre-crack, a) normalized by propagation toughness, $\mathscr{G}_{\mathrm{Ic,p}}$ and b) normalized by the $\mathscr{R}$-curve as a function of the delaminated length, $\mathscr{G}_{\mathrm{IC},\mathscr{R}} = \mathrm{f}(\mathrm{a} - \mathrm{a}_0)$.

propagation fracture toughness $\mathscr{G}_{Ic,p}$ (Fig. 8a). If the applied strain energy release rate $\mathscr{G}_{max}$ is normalized by the $\mathscr{R}$-curve as a function of the delaminated length, $\mathscr{G}_{IC,\mathscr{R}} = f(a - a_0)$ (Fig. 8b) [6,38], the propagation curve of tests run from insert collapsed over the tests run from pre-crack but they still showed divergence in the slope of the propagation law (exponent m), evidencing higher crack growth rate in tests run from insert. This divergence may be attributed to the fact that fracture process zone evolves under fatigue loading conditions during the propagation tests run from insert. Therefore, since failure mechanisms such as plastic deformation and fibre bridging are developed under fatigue conditions, the $\mathscr{R}$-curve effects may be different compared to the ones tested from a statically developed fracture process zone. These results are coherent with the work reported in [10], where different fatigue propagation curves were obtained in specimens that exhibited fibre bridging, propagating at higher crack growth rate tests run from fatigue pre-crack compared to tests run from static pre-crack. Also, the curves obtained from different severity did not collapse in a single curve.

To compare the fatigue propagation behaviour of AS4D/PEKK-FC thermoplastic with a high-performance thermoset [22], both fatigue propagation behaviours are similar proportionally to their fracture toughness. However, if $\mathscr{G}_{\max}$ is not normalized by the toughness of the material $\mathscr{G}_{IC,\mathscr{R}}$, AS4D/PEKK-FC thermoplastic show a slower crack growth than thermosets at the same $\mathscr{G}_{\max}$.

5. Numerical modelling

5.1. Verification of the fatigue parameter determination method

After applying the fatigue parameter determination method described in section 3.4, the fatigue parameters presented in Table 9 were obtained. To verify the accuracy of the method, the model was numerically calculated with the fatigue parameters set in Table 9, and the onset and propagation responses were compared with the experimental constants (Table 10). With all the fatigue law superposition architectures a good numerical representation of the fatigue onset and propagation was achieved for the range where fatigue data is available. The graphical representation of the numerical correlation with the experimental data can be seen in Fig. 9.

It can be seen that in the case of superposition architecture 1, after an initial transient zone, crack propagates in a self-similar way, resulting in a single propagation law (eq. (10). In contrast, fatigue propagation of architectures 2 and 3 cannot be modelled by a single propagation law. This is because as the damaged area evolves, the different fatigue parameters have an impact in the global fatigue damage rate. Therefore, the range where experimental data is available was used to extract the numerical fatigue propagation constants.

Table 9
Obtained fatigue parameters considering fatigue onset and propagation data:

	ε [–]	p [–]	η_A [–]	η_B [–]
Superposition architecture 1	0.1487	$\beta + 2.56$	0.932	–
Superposition architecture 2	0.0687	$\beta - 1.28$	0.895	–
Superposition architecture 3	0.0402	$\beta - 2.14$	0.907	0.689

Table 10
Verification of the fatigue parameter determination method.

	O_A [mm/N]	O_B [–]	Fatigue onset R^2[–]	m_I [–]	C_I [mm/cycle]	Fatigue Propagation R^2[–]
Experimental	2.81E-5	4.57E-1	–	8.87	9.32E1	–
Superposition architecture 1	4.26E-5	4.42E-1	0.95	8.54	5.15E2	0.99
Superposition architecture 2	4.54E-5	4.43E-1	0.98	8.87	3.13E1	0.99
Superposition architecture 3	4.55E-5	4.41E-1	0.96	8.93	6.22E2	0.99

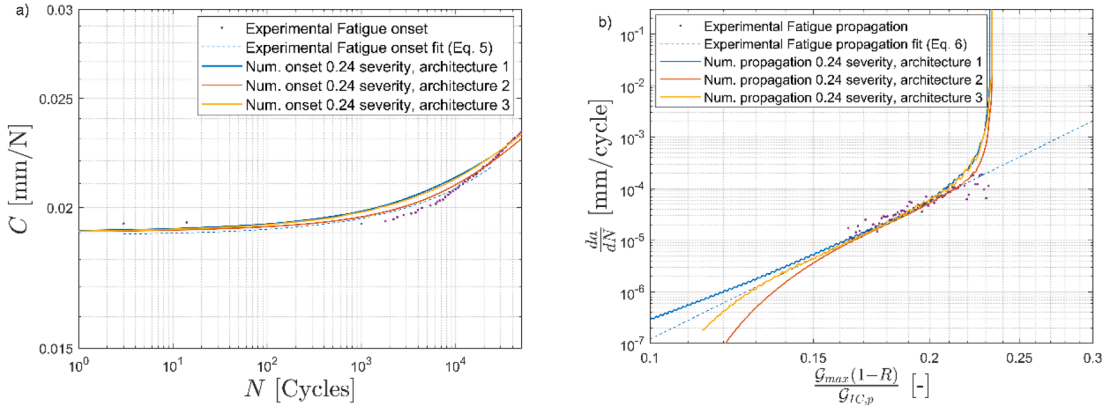

Fig. 9. Verification of fatigue parameter determination method for different fatigue damage accumulation architectures: a) onset and b) propagation.

5.2. *Numerical modelling of fatigue $\mathscr{R}$-curve effects*

In this section, the rest of the mode I fatigue tests from insert (Table 2) were simulated with the fatigue input sets given in Table 9 and are plotted in Fig. 10.

The propagation curves obtained with fatigue law superposition architecture 1 tend to collapse in a single crack propagation law (Eq. (10) (Fig. 10b). Since the numerical model tends to predict self-similar propagation after the first transient region, the model is not able to achieve a big enough offset between propagation laws, resulting in overestimation of crack growth rates for high severity specimens and underestimation in low severity specimen. Likewise, the predicted fatigue onset at higher severities is more rapid than the experimental data, and slower at low severities (Fig. 10a). Therefore, it is demonstrated that imposing the same fatigue damage accumulation law in all the superposed cohesive laws does not yield accurate enough predictions for composite materials with ductile fracture and large-scale bridging.

With the fatigue law superposition architecture 2 the propagation curves do not collapse in a single Paris law thanks to assuming no fatigue damage in the cohesive laws that model low density long fibre bridging. Instead, fatigue crack growth rate gradient decreases in log-log scale as crack length increases (Fig. 10d). This is because as the damaged area extends, dissimilar fatigue damage accumulation is promoted as FCL 4 and 5 do not accumulate fatigue damage. This way, the offset in crack growth rate between specimens tested at different severities is captured with greater accuracy than with architecture 1. However, this cohesive law superposition architecture is not fully able to capture the whole offset between propagation curves, resulting in overestimation of crack growth rates for high severity specimens and underestimation in low severity specimen.

Experimental data for fatigue onset of the specimens tested at load severities of 0.3 and above, experienced a sudden increase in their compliance at 300 cycles (Fig. 10c). Since this event cannot be modelled, numerical results should follow the onset experimental data with an offset towards the right-hand side of the X axis. Therefore, fatigue onset predictions made with architecture 2 at higher severities result in a faster onset than expected, and slower at low severities.

When fatigue parameters were allowed to be independent in all the superposed cohesive laws (superposition architecture 3), fatigue propagation of different loading severities was accurately predicted (Fig. 10e, Fig. 10f).

Moreover, it can be learned from numerical data that the experimental range characterized at each severity is governed by different failure mechanisms. For example, since longer crack lengths were obtained in specimens tested at higher severities (specimens with severities of 0.43 and 0.38), the experimental propagation laws were first governed by matrix crack resistance, resulting in flatter propagation laws. As damage was extended, other failure mechanisms were activated resulting in a steeper propagation law. On the contrary, at severities where there was not much damage extension (severities of 0.24 and 0.14), only the propagation law dominated by matrix resistance was characterized.

Finally, the accuracy of the proposed superposition architecture 3 was validated by comparing the numerical fatigue delamination growth length a vs the number of cycles N (Fig. 11). The maximum obtained mismatch was 0.5 mm of delamination length within the whole experimental test range over all the analysed fatigue severities if the sudden compliance increase in the 0.43 and 0.38 tests is excluded.

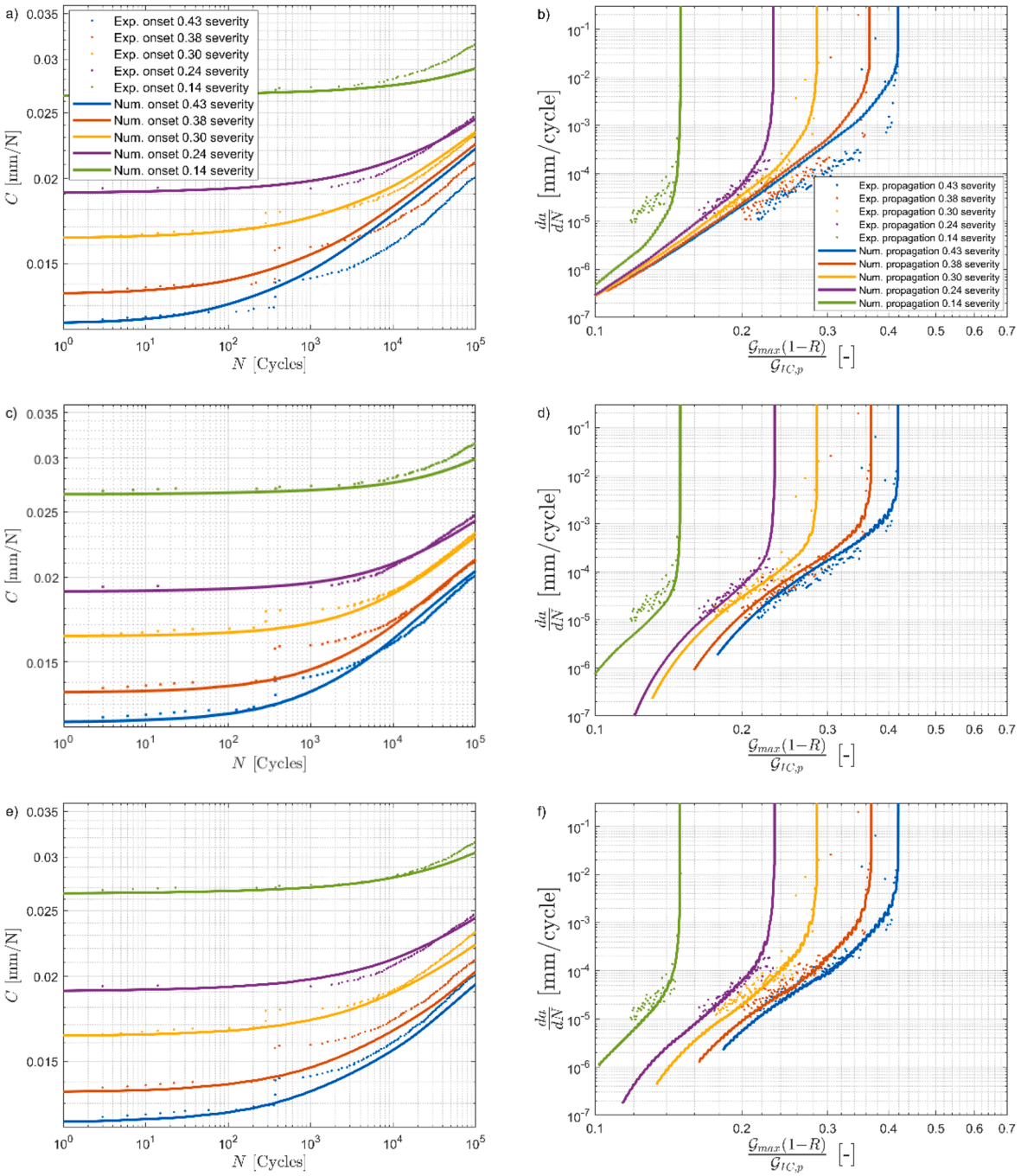

Fig. 10. Fatigue $\mathscr{R}$-curve effect modelling under mode I loading, (a, c, e) fatigue onset for damage accumulation architectures 1–3, (b, d, f) fatigue propagation for damage accumulation architectures 1–3 respectively.

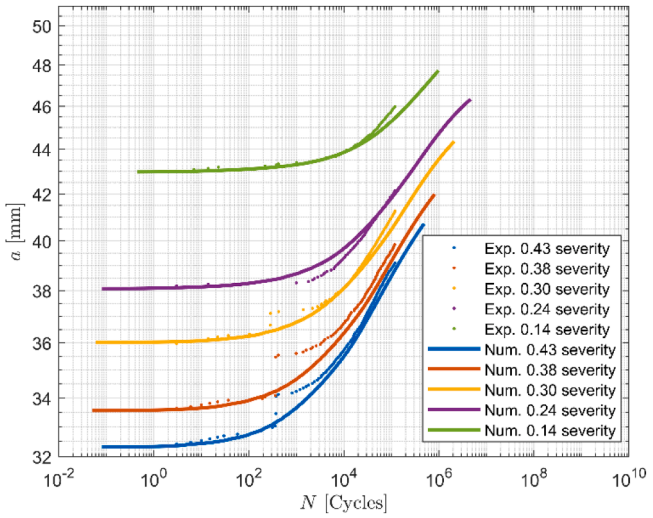

Fig. 11. Validation of the superposition architecture 3 by comparing the numerical fatigue delamination growth length a vs the fatigue cycle number N.

6. Conclusions

In the present work the fatigue onset and propagation behaviour of a AS4D/PEKK-FC thermoplastic material has been studied under mode I loading. Fatigue onset and propagation characterization has been performed, reducing the testing costs by using a multi-fatigue testing rig that allows loading 6 specimens at the same time. Compared to other material systems, the fatigue onset and propagation performance of AS4D/PEKK-FC thermoplastic is superior to a high performance thermoset [22] proportionally to the fracture toughness of the material, $\mathscr{G}_{IC,\mathscr{R}}$.

The fatigue onset resistance of the material is a function of the $\mathscr{R}$-curve behaviour observed under static loading caused by the presence of energy dissipating mechanisms such as plastic deformation and large-scale bridging. Therefore, the fatigue onset curve ($\mathscr{G}_{max}vsN$) collapse to a single curve when normalizing the applied energy release rate accounting for the static $\mathscr{R}$ -curve effects ($\mathscr{G}_{max}/\mathscr{G}_{IC,\mathscr{R}}vsN$).

For the fatigue propagation behaviour, an offset in the crack growth rate curves when tested at different severities was observed. Moreover, the propagation curves obtained from specimens run from insert do not collapse over the tests run from pre-crack even if the strain energy values are normalized by the $\mathscr{R}$-curve as a function of the delaminated length, $\mathscr{G}_{IC,\mathscr{R}}$. This may be explained by assuming that the development of the failure mechanisms under static or fatigue loading is different.

The experimental findings remark the need of developing a simulation strategy to account for $\mathscr{R}$-curve effects under fatigue loading, such as the offset in the crack growth curves. This implies analysing how to accumulate fatigue damage. In this work, a simulation strategy for a fatigue cohesive zone model was developed, based on multiple superposition of cohesive laws and determination of fatigue model parameters based on experimental fatigue onset and propagation data. Different fatigue accumulation architectures within the superposed cohesive laws were proposed to get a better understanding on how fatigue damage evolves in materials with ductile fracture and large-scale bridging. It is concluded that assuming the same fatigue damage accumulation law for all the superposed cohesive laws does not yield accurate predictions. Instead, fatigue parameters in the model must allow independent fatigue damage accumulation rates to the superposed cohesive laws. This conclusion agrees with the assumption that the superposed cohesive laws model different failure mechanisms, and each of this failure mechanism can accumulate damage at different rates under fatigue loading.

It has been demonstrated that the proposed simulation strategy makes a phenomenological predictive tool able to model both static and fatigue $\mathscr{R}$-curve effects under mode I loading.

CRediT authorship contribution statement

I. Leciñana: Writing – original draft, Validation, Software, Methodology, Conceptualization. **J. Renart:** Writing – review & editing, Writing – original draft, Supervision, Resources, Methodology, Investigation, Conceptualization. **A. Turon:** Writing – review & editing, Supervision, Resources, Methodology, Conceptualization. **J. Zurbitu:** Writing – review & editing, Supervision, Resources, Conceptualization. **B.H.A.H. Tijs:** Writing – review & editing, Validation, Supervision, Software, Resources, Methodology, Conceptualization.

Declaration of Competing Interest

The authors declare that they have no known competing financial interests or personal relationships that could have appeared to influence the work reported in this paper.

Data availability

Data will be made available on request.

Acknowledgements

This work has been partially funded by the Spanish Government (Ministerio de Ciencia e Innovacion) under contract PID2021-127879OB-C21. The last author received co-funding from the Clean Sky 2 Joint Undertaking (JU) under grant agreement No 945583 (project STUNNING). The JU receives support from the European Union's Horizon 2020 research and innovation programme and the Clean Sky 2 JU members other than the Union.

References

[1] International, *ASM Handbook Volume 21: Composites*. ASM International. 2001.
[2] Hojo M, Gustafson C, Tanaka K, Hayashi R. Mode I Propagation of Delamination Fatigue Cracks in CFRP. Adv Mater Sev Serv Appl 1990:353–72. https://doi.org/10.1007/978-94-009-3445-0_23.
[3] Brunner AJ, Murphy N, Pinter G. Development of a standardized procedure for the characterization of interlaminar delamination propagation in advanced composites under fatigue mode I loading conditions. Eng Fract Mech 2009;76(18):2678–89. https://doi.org/10.1016/j.engfracmech.2009.07.014.
[4] Stelzer S, Brunner AJ, Argüelles A, Murphy N, Pinter G. Mode I delamination fatigue crack growth in unidirectional fiber reinforced composites: Development of a standardized test procedure. Compos Sci Technol 2012;72(10):1102–7. https://doi.org/10.1016/j.compscitech.2011.11.033.
[5] Stelzer S, Brunner AJ, Argüelles A, Murphy N, Cano GM, Pinter G. Mode I delamination fatigue crack growth in unidirectional fiber reinforced composites: Results from ESIS TC4 round-robins. Eng Fract Mech 2014;116:92–107. https://doi.org/10.1016/j.engfracmech.2013.12.002.
[6] Murri GB. Effect of data reduction and fiber-bridging on Mode i delamination characterization of unidirectional composites. J Compos Mater 2014;48(19):2413–24. https://doi.org/10.1177/0021998313498791.
[7] Tijs BHAH, Abdel-Monsef S, Renart J, Turon A, Bisagni C. Characterization and analysis of the interlaminar behavior of thermoplastic composites considering fiber bridging and R-curve effects. Compos Part A Appl Sci Manuf 2022;162:107101. https://doi.org/10.1016/j.compositesa.2022.107101.
[8] Solvay, "APC (PEKK-FC) PEKK-FC thermoplastic polymer prepreg." 2022. APC (PEKK)/AS4D.
[9] Brunner AJ. "Scatter, Scope and Structures: What fatigue fracture testing of fiber polymer composites is all about", *IOP Conf. Ser.* Mater Sci Eng 2018;388(1):pp. https://doi.org/10.1088/1757-899X/388/1/012003.
[10] Yao L, Alderliesten R, Zhao M, Benedictus R. Bridging effect on mode i fatigue delamination behavior in composite laminates. Compos Part A Appl Sci Manuf 2014;63:103–9. https://doi.org/10.1016/j.compositesa.2014.04.007.
[11] Yao L, Alderliesten RC, Jones R, Kinloch AJ. Delamination fatigue growth in polymer-matrix fibre composites: A methodology for determining the design and lifing allowables. Compos Struct 2018;196(May):8–20. https://doi.org/10.1016/j.compstruct.2018.04.069.
[12] Alderliesten RC, Brunner AJ, Pascoe JA. Cyclic fatigue fracture of composites: What has testing revealed about the physics of the processes so far? Eng Fract Mech 2018;203(June):186–96. https://doi.org/10.1016/j.engfracmech.2018.06.023.
[13] Alderliesten R. "Fatigue delamination of composite materials - Approach to exclude large scale fibre bridging", *IOP Conf. Ser.* Mater Sci Eng 2018;388(1). https://doi.org/10.1088/1757-899X/388/1/012002.
[14] B.H.A.H. Tijs et al., Virtual testing of thermoplastic composites: Towards a hybrid simulation-physical testing pyramid, *ECCM 2018 - 18th Eur. Conf. Compos. Mater.* 2018.
[15] Carreras L, Turon A, Bak BLV, Lindgaard E, Renart J, Martin de la Escalera F, et al. A simulation method for fatigue-driven delamination in layered structures involving non-negligible fracture process zones and arbitrarily shaped crack fronts. Compos Part A Appl Sci Manuf 2019;122:107–19.
[16] Carreras L, Bak BLV, Turon A, Renart J, Lindgaard E. Point-wise evaluation of the growth driving direction for arbitrarily shaped delamination fronts using cohesive elements. Eur J Mech A Solids 2018;72:464–82.
[17] Carreras L, Lindgaard E, Renart J, Bak BLV, Turon A. An evaluation of mode-decomposed energy release rates for arbitrarily shaped delamination fronts using cohesive elements. Comput Methods Appl Mech Eng 2019;347:218–37. https://doi.org/10.1016/j.cma.2018.12.027.
[18] I. Lecinana, J. Zurbitu, J. Renart, A. Turon, and L. Carreras, Global sensitivity analysis of an S-N curve-based fatigue cohesive zone model and validation through a benchmark test, *20th Eur. Conf. Compos. Mater. ECCM20*, 2022.
[19] Dávila CG. From S-N to the Paris law with a new mixed-mode cohesive fatigue model for delamination in composites. Theor Appl Fract Mech 2020;106:102499.
[20] C.G. Dávila, C.A. Rose, G.B. Murri, W.C. Jackson, W.M. Johnston, Evaluation of fatigue damage accumulation functions for delamination initiation and propagation, *Nasa/Tp–2020-220584*, no. April, 2020.
[21] Lecinana I, Zurbitu J, Renart J, Turon A. A robust fatigue parameter determination method for a fatigue Cohesive Zone Model based on S-N curves. Int J Fatigue 2023;171(February):2023. https://doi.org/10.1016/j.ijfatigue.2023.107582.
[22] Renart J, Budhe S, Carreras L, Mayugo JA, Costa J. A new testing device to simultaneously measure the mode I fatigue delamination behavior of a batch of specimens. Int J Fatigue 2018;116(June). https://doi.org/10.1016/j.ijfatigue.2018.06.021.
[23] Renart J, Blanco N, Pajares E, Costa J, Lazcano S, Santacruz G. Side Clamped Beam (SCB) hinge system for delamination tests in beam-type composite specimens. Compos Sci Technol 2011;71(8):1023–9. https://doi.org/10.1016/j.compscitech.2010.10.005.
[24] Turon A, González EV, Sarrado C, Guillamet G, Maimí P. Accurate simulation of delamination under mixed-mode loading using a cohesive model with a mode-dependent penalty stiffness. Compos Struct 2018;184:506–11.
[25] Benzeggagh ML, Kenane M. Measurement of mixed-mode delamination fracture toughness of unidirectional glass/epoxy composites with mixed-mode bending apparatus. Compos Sci Technol 1996;56:439–49. https://doi.org/10.1016/0266-3538(96)00005-X.
[26] Abdel Monsef S, Ortega A, Turon A, Maimí P, Renart J. An efficient method to extract a mode I cohesive law for bonded joints using the double cantilever beam test. Compos Part B Eng 2019;178(June):107424. https://doi.org/10.1016/j.compositesb.2019.107424.
[27] Abdel Monsef S, Pérez-Galmés M, Renart J, Turon A, Maimí P. The influence of mode II test configuration on the cohesive law of bonded joints. Compos Struct 2020;234. https://doi.org/10.1016/j.compstruct.2019.111689. August 2019.
[28] Teimouri F, Heidari-Rarani M, Haji Aboutalebi F. Finite element modeling of mode I fatigue delamination growth in composites under large-scale fiber bridging. Compos Struct 2021;263(February):113716. https://doi.org/10.1016/j.compstruct.2021.113716.
[29] Joosten MW, Dávila CG, Yang Q. Predicting fatigue damage in composites subjected to general loading conditions. Compos Part A Appl Sci Manuf 2022;156(February). https://doi.org/10.1016/j.compositesa.2022.106862.

[30] Dávila CG. From S-N to the Paris law with a new mixed-mode cohesive fatigue model for delamination in composites. Theor Appl Fract Mech 2020;106(June). https://doi.org/10.1016/j.tafmec.2020.102499.
[31] Yin S, Gong Y, Li W, Zhao L, Zhang J, Hu N. A novel four-linear cohesive law for the delamination simulation in composite DCB laminates. Compos Part B Eng 2020;180:107526. https://doi.org/10.1016/j.compositesb.2019.107526.
[32] Dávila CG, Rose CA, Camanho PP. A procedure for superposing linear cohesive laws to represent multiple damage mechanisms in the fracture of composites. Int J Fract 2009;158(2):211–23. https://doi.org/10.1007/s10704-009-9366-z.
[33] Liu H, Ong YS, Cai J. A survey of adaptive sampling for global metamodeling in support of simulation-based complex engineering design. Struct Multidiscip Optim 2018;57(1):393–416. https://doi.org/10.1007/s00158-017-1739-8.
[34] Wang GG, Shan S. Review of metamodeling techniques in support of engineering design optimization. J Mech Des Trans ASME 2007;129(4):370–80. https://doi.org/10.1115/1.2429697.
[35] Krige DG. A statistical approach to some basic mine valuation problems on the Witwatersrand. J South African Inst Min Metall 1951;52(6):119–39.
[36] Deb K, Pratap A, Agarwal S, Meyarivan T. A fast and elitist multiobjective genetic algorithm: NSGA-II. IEEE Trans Evol Comput 2002;6(2):182–97. https://doi.org/10.1109/4235.996017.
[37] ASTM International, "ASTM D6115-97(2004), Standard Test Method for Mode I Fatigue Delamination Growth Onset of Unidirectional Fiber-Reinforced Polymer Matrix Composites." West Conshohocken, PA, 2004, doi: 10.1520/D6115-97R19.
[38] Yao L, Alderliesten RC, Benedictus R. The effect of fibre bridging on the Paris relation for mode I fatigue delamination growth in composites. Compos Struct 2016;140:125–35. https://doi.org/10.1016/j.compstruct.2015.12.027.